Mechanically Induced Titin Kinase Activation Studied by Force-Probe Molecular Dynamics Simulations

Frauke Gräter,*[†] Jianhua Shen,[†] Hualiang Jiang,[†] Mathias Gautel,[‡] and Helmut Grubmüller*

*Theoretical and Computational Biophysics Department, Max-Planck-Institute for Biophysical Chemistry, 37077 Göttingen, Germany; [†]Drug Discovery and Design Center, Shanghai Institute of Materia Medica, Chinese Academy of Sciences, Shanghai 201203, China; and [‡]Cardiovascular Research Division and The Randall Division, King's College London, London SE1 1UL, Great Britain

ABSTRACT The conversion of mechanical stress into a biochemical signal in a muscle cell requires a force sensor. Titin kinase, the catalytic domain of the elastic muscle protein titin, has been suggested as a candidate. Its activation requires major conformational changes resulting in the exposure of its active site. Here, force-probe molecular dynamics simulations were used to obtain insight into the tension-induced activation mechanism. We find evidence for a sequential mechanically induced opening of the catalytic site without complete domain unfolding. Our results suggest the rupture of two terminal β-sheets as the primary unfolding steps. The low force resistance of the C-terminal relative to the N-terminal β-sheet is attributed to their different geometry. A subsequent rearrangement of the autoinhibitory tail is seen to lead to the exposure of the active site, as is required for titin kinase activity. These results support the hypothesis of titin kinase as a force sensor.

INTRODUCTION

Muscle is composed of mainly three types of protein filaments: myosin, actin, and titin. The motor proteins myosin and actin undertake the task of generating an active force for muscle contraction, whereas titin plays a major role in muscle elasticity (Linke and Fernandez, 2002). Titin is a protein of ~3 MDa, spanning half the sarcomere from the Z-line to the M-band, thereby connecting the other two major muscle filaments, actin and myosin, with each other, as shown in Fig. 1 (Tskhovrebova and Trinick, 2003). It is mainly composed of ~300 repeating amino acid modules of immunoglobulin (Ig) and fibronectin III (Fn3) classes with insertions of unique domains (Labeit and Kolmerer, 1995). Upon muscle cell stretch, the titin filament generates passive tension by straightening and partial unfolding of its domains that restores the sarcomere length and realigns the muscle filaments after stress release (Trinick and Tskhovrebova, 1999).

Single-molecule studies of the mechanical stability and mechanical unfolding of titin have revealed the molecular basis of titin elasticity. I-band Ig and Fn3 domains have been extensively studied by optical tweezers and atomic force microscopy (AFM) experiments (Tskhovrebova et al., 1997; Kellermayer et al., 1997; Rief et al., 1997; Li et al., 2002; Fowler et al., 2002) and molecular dynamics (MD) simulations (Lu et al., 1998; Paci and Karplus, 1999; Isralewitz et al., 2001; Rief and Grubmüller, 2002). Hydrogen bond ruptures between terminal β-strands as initial events of Ig unfolding lead to an unfolding intermediate, which upon further pulling unfolds in an all-or-none fashion (Marszalek et al., 1999; Lu and Schulten, 2000). The high rupture forces

required for Ig and Fn3 unfolding found in these experiments indicate that unfolding, if any, occurs only under extreme physiological tension to prevent irreversible damage (Linke and Fernandez, 2002; Williams et al., 2003).

Near titin's carboxy terminus, located at the M-band, titin contains its only catalytic domain, the titin kinase (Fig. 1). A crystal structure of the titin kinase domain has been solved (Mayans et al., 1998) and shows a kinase domain fold that, with a β-sheet-rich smaller lobe and an α-helix-rich bigger lobe, is typical for giant kinases and was first found for cAPK (Bossemeyer et al., 1993). In contrast to most other kinases, titin kinase is autoinhibited by its C-terminal regulatory tail (shown in *red*), in a way similar to twitchin kinase (Kobe et al., 1996). The αR2 helix binds to the kinase ATP binding site and specifically interacts with the residues involved in catalysis. The C-terminal part of the regulatory tail, βR1, forms a β-sheet with βC10 and βC11. Titin kinase activation therefore requires release of autoinhibition, in particular the removal of the autoinhibitory tail from the active site. It has been shown to occur in differentiating myocytes upon phosphorylation of Tyr[170] and Ca^{2+}/calmodulin binding to αR1, the N-terminal α-helix of the regulatory tail (Mayans et al., 1998).

The role of titin kinase has been partly uncovered by experiments showing that it influences myofibrillogenesis in differentiating muscle cells by phosphorylation of telethonin (Mayans et al., 1998; Nicholas et al., 2002). Deletion of a large segment of M-line titin, including the binding sites for muscle-specific ring finger proteins (MURF), myomesin, and a down-regulated rhabdomyocytes LIN-domain (DRAL) as well as titin kinase, indeed leads to low expression and poor organization of myofibrils (Miller et al., 2003; Gotthardt et al., 2003). Studies indicating an interaction of titin kinase with MURF point at a role of titin kinase in muscle gene expression signaling in adult muscle
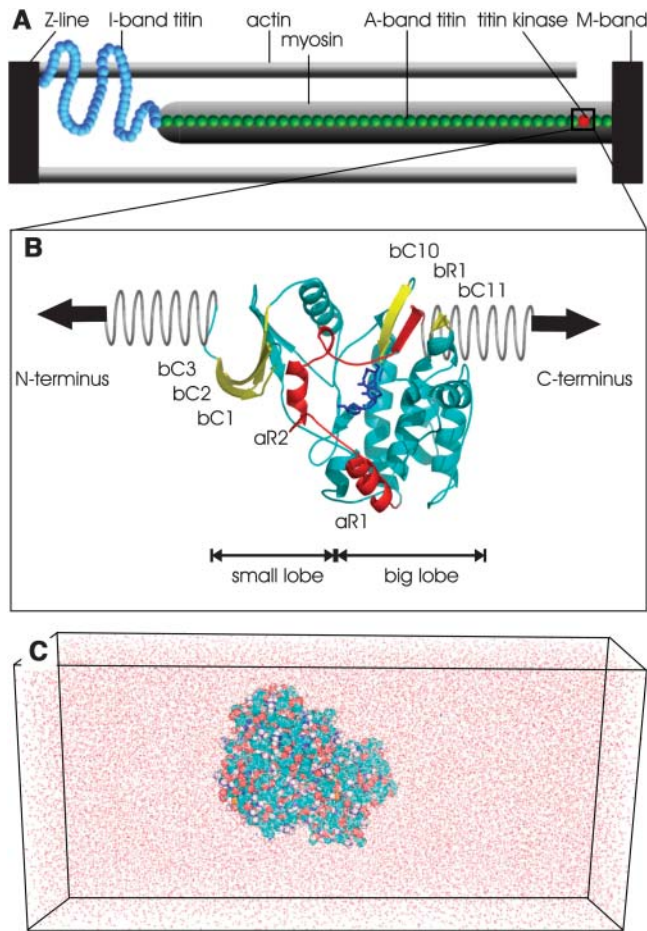
FIGURE 1 Physiological role, structure, and simulation setup of titin kinase. (*a*) Half of the sarcomere and the position of titin kinase (*red*) are sketched. Tandem titin domains are shown as spheres. (*b*) Titin kinase (1TKI) (Mayans et al., 1998) in its autoinhibited conformation. The catalytic site is shown in blue, the regulatory tail in red, and the terminal β-sheets in yellow. The harmonic pulling potentials used for the force-probe simulations described in the Methods section are symbolized as springs. (*c*) Simulation system of the FPMD simulations. All proteins were plotted with Pymol (DeLano, 2001).

(Centner et al., 2001; McElhinny et al., 2002; Pizon et al., 2002).

Considering the exceptional location of the kinase, which as titin constituent is integrated into the molecular spring, we speculated that titin might play the role of a force sensor that passes the information of stress level in the titin filament on via substrate phosphorylation. In this scenario, one has to assume that the structural rearrangements in the titin kinase domain are driven by the stretching forces in titin. Whether this is actually the case and how kinase activation is triggered by release of autoinhibition is the subject of this work. To this aim, we have carried out force-probe molecular dynamics (FPMD) simulations (Grubmüller et al., 1996; Izrailev et al., 1997) of titin kinase partial unfolding by subjecting both titin kinase termini to a harmonic pulling

potential which mimics the tension in a stretched titin filament. The simulations aim at a), estimating the force required for mechanical unfolding, b), examining the force-induced structural changes in the regulatory tail and kinase domain with regard to kinase activity, and c), gaining a closer insight into the dependence of force resistance on structural properties.

METHODS

MD and force-probe MD simulations

All simulations were carried out using the MD software package GROMACS 3.1.4 (Lindahl et al., 2001). The GROMOS96 force field (van Gunsteren et al., 1996) for the protein and the SPC water model (Berendsen et al., 1981) were employed. Simulations were run in the NPT ensemble. The temperature was kept constant at $T = 300$ K by coupling to a Berendsen thermostat with a coupling time of $\tau_T = 0.1$ ps (Berendsen et al., 1984). The pressure was kept constant at $p = 1$ bar using anisotropic coupling to a Berendsen barostat with $\tau_p = 1.0$ ps and a compressibility of $4.5 \ 10^{-5} \ \text{bar}^{-1}$ in x, y, and z direction (Berendsen et al., 1984). All bonds were constrained using the LINCS algorithm (Hess et al., 1997). An integration time step of 2 ps was used. Lennard-Jones interactions were calculated using a cutoff of 10 Å. At a distance smaller than 10 Å, electrostatic interactions were calculated explicitly, whereas long-range electrostatic interactions were calculated by particle-mesh Ewald summation (Darden et al., 1993).

The simulation system was set up as follows. Protonation states of titratable groups of titin kinase (Protein Data Bank entry 1TKI (Mayans et al., 1998)) were determined by calculating pKa values using Whatif (Vriend, 1990) and its interface to DelPhi (Nicholls et al., 1990). The protein was solvated in a cubic box of $88 \times 78 \times 76 \ \text{Å}^3$ in size containing ~50,000 atoms. Added were 27 sodium and 29 chloride ions corresponding to a physiological ion strength of 100 mM. An energy minimization of 200 steps using the steepest descent algorithm was followed by a 400 ps MD simulation with harmonical constraints on the protein heavy atoms with a force constant of $k = 1000 \ \text{kJ mol}^{-1} \ \text{nm}^{-2}$ to equilibrate water and ions. A subsequent MD simulation of 7.5 ns length was performed to equilibrate the whole system, during which the protein backbone root mean-square deviation (RMSD) was monitored.

For FPMD simulations, a simulation system large enough to accommodate the unfolded protein is required. After rotating the equilibrated system such that the termini were aligned along the box z axis, water and ions were added to give a cuboid box of $78 \times 84 \times 186 \ \text{Å}^3$ in size, containing ~120,000 atoms (see Fig. 1). A subsequent 200 ps MD simulation with harmonic constraints on the protein heavy atoms during the first 100 ps was carried out. The final structure of this run served as the starting structure for the FPMD simulations.

Each of the C_α atoms of the two terminal amino acids (N, C) were subjected to a harmonic spring potential,

$$V_{\text{spring,i}}(t) = k_0[z_i(t) - z_{\text{spring,i}}(t)]^2, \tag{1}$$

with $i = $ N, C, where $k_0 = 500 \ \text{kJ mol}^{-1} \ \text{nm}^{-2}$ is the force constant of the springs, $z_i(t)$ the position of the pulled C_α atoms, and $z_{\text{spring,i}}(t)$ the position of the springs. This ''two-side pulling'' approach differs from the usual FPMD simulations where only one terminus is pulled and the other one is held fixed. This has the advantage that friction due to dragging the protein through water should be significantly reduced.

Mechanical stress was applied by moving the two springs with constant velocity v in opposite directions, $z_{\text{spring,i}}(t) = z_i(0) \pm \Delta z(t)$, where $\Delta z(t) = vt$ is the spring dislocation. Forces

$$F_i = k_0[z_i(t) - z_{\text{spring,i}}(t)] \tag{2}$$

at the two pull groups (i = N, C) were recorded every time step.

A number of FPMD simulations with different pulling velocities v were performed, 0.004 Å/ps, 0.008 Å/ps, 0.02 Å/ps (twice), 0.05 Å/ps (twice), 0.1 Å/ps, and 0.5 Å/ps, with simulation times ranging from 150 ps to 22 ns, totaling 42 ns of FPMD simulation time.

Simulations were stopped after the distance of one of the termini to the box borders dropped below 7 Å. To further extend the FPMD simulations of 0.004 Å/ps and 0.008 Å/ps pulling velocity, pulling was continued with truncated protein structures, and the elasticity of the omitted peptides was described by a wormlike chain (wlc) model. Here, residues 1–19 and 308–321 of the final snapshots with $\Delta z_i(t)$ = 65 Å obtained from the 0.008 Å/ps and 0.004 Å/ps simulations were deleted. Terminal ammonium and carboxylate groups of residues 20 and 307, respectively, were built, and SPC water and two sodium ions to substitute the net negative charge of the removed peptide chains were added. The resulting system was energy minimized, and solvent and ions equilibrated with harmonic restraints on the protein heavy atoms as described above. C_α atoms of residues 20 and 307 were then subjected to a harmonic spring potential with modified spring constant k_0' to account for the elasticity of the deleted peptide chains. Accordingly, k_0' was calculated from the force F_{wlc} present at the peptide fragments alone using the wlc model with

$$k_0' = \frac{F_{wlc}}{\Delta d} = \frac{k_B T}{p \Delta d}\left[\frac{1}{4(1 - x/L)} - \frac{1}{4} + \frac{x}{L}\right], \quad (3)$$

where Δd denotes the end-to-end distance of the peptide chain, k_B the Boltzmann constant, T the temperature, and p = 0.4 nm (Rief et al., 1997) the persistence length. The contour length L was chosen as the number of amino acids times length of one amino acid. The resulting spring constant of ~100 kJ/mol/nm^2 for the deleted peptide chains is smaller than k_0, and thus was chosen as the spring constant k_0' for further pulling.

The titin kinase construct used for crystallization (Mayans et al., 1998) lacks 24 N-terminal residues of the kinase domain. This sequence is resolved in the twitchin kinase crystal structure (Protein Data Bank entry 1KOB (Kobe et al., 1996)) and shows high sequence similarity in these two proteins (Fig. 2). To check if the missing part of titin kinase affects the results, additional MD and FPMD simulations of twitchin kinase were performed. The simulation setup was chosen similar to the setup of titin kinase. The structure was solvated in SPC water with physiological ion strength in a cubic box of 101 × 80 × 83 Å^3 in size. After energy minimization and a 400 ps MD simulation with harmonic constraints on the protein heavy atoms, a 5.5 ns equilibration run of the whole system was performed. The 74 × 85 × 140 Å^3 box for the subsequent FPMD simulation contained the equilibrated twitchin kinase structure, with its termini aligned along the z axis, water, and ions (~89,000 atoms). Added water and ions were equilibrated in a 200 ps MD simulation as described above. A single FPMD simulation of 6 ns in length was performed, as also described above, with two pull groups, the C_α atoms of residues 1 and 353, a pulling velocity of 0.008 Å/ps, and a spring constant of 500 kJ/mol/nm^2.

Force profiles were obtained using Eq. 2 and smoothened with a Gaussian function of 1.6 Å width to suppress artificial fluctuations at the resonance frequency of the spring. Unfolding forces were determined as the maxima of the force profiles. Maximal forces taken from profiles that have been smoothened with widths of 0.4 Å and 6.4 Å, respectively, served as an estimate for the uncertainty introduced by choosing the smoothing width (Grubmüller et al., 1996).

Protein domains and the hinge axis involved in the hinge motion as obtained from principal component analysis were determined using the program DynDom (Hayward and Berendsen, 1998).

Hydrogen bond potentials were calculated from hydrogen-acceptor distances Δs according to

$$E_{pot} = -\frac{1}{2}(50 \times 10^{-3} \text{ kJ/mol})e^{-36\Delta s} \quad (4)$$

(Espinosa et al., 1998). To obtain a measure for the width of the hydrogen bond potential decay, a_0, hydrogen bond energy traces were fitted with the function $E_{pot}(\Delta z) = [\exp(\Delta z - a_2)/a_0 + a_1]^{-1}$, where Δz is the distance between the current and initial location of the spring.

Force-probe Monte Carlo simulations

To aid the interpretation of the obtained force profiles, and, in particular of the observed β-sheet dissociation, two-dimensional models of the traversed energy landscapes were studied by force-probe Monte Carlo (FPMC) simulations. The rupture of the two β-sheets with six interstrand hydrogen bonds each was modeled using a properly chosen two-dimensional effective potential $G(x_1, x_2)$ (see Results section and Fig. 9 there). The two reaction coordinates x_1 and $x_2 - x_1$ were defined as the distances between the terminal amino acids of the β-strands departing concurrently or sequentially, respectively. The total length of the two connected β-sheets then is given by x_2. The origin was chosen such that the initial β-sheet lengths were zero.

A harmonic spring potential as a function of the spring position and x_2 was added in a similar manner as in the FPMD simulations (Eq. 1), using the same spring constant of 500 kJ/mol/nm^2. The short peptide sequences between the terminal sheets and the spring in the FPMD simulations are absent in the MC simulations. To take their elasticity into account, their force constants were calculated according to Eq. 3 as described above, but were found to be an order of magnitude larger than the force constant of the spring, and thus to be negligible. Each MC simulation was started with a particle at the minimum of the energy surface $G(x_1, x_2)$ (reaction coordinate x_1 = 0 and $x_2 - x_1$ = 0). Random Gaussian distributed steps backward and forward along the two reaction coordinates x_1 and $x_2 - x_1$ with an average step size of 0.0015 nm were accepted or rejected according to the Metropolis criterion (Metropolis et al., 1953) at 300 K. Each step was accompanied by a movement of the spring to a larger x_2 with a constant step size. A set of FPMC simulations with spring velocities varying between 10^{-5} and 10^{-2} nm/step was performed, and the spring position at which the β-sheets rupture was monitored.

RESULTS

Equilibration and free dynamics

The structure of titin kinase during equilibration and the subsequent 7.5 ns long free MD simulation was compared to the crystal structure. The RMSD from the crystal structure leveled off at 2.0 Å for the protein backbone atoms. The root mean-square fluctuations per residue showed a correlation coefficient = 0.7 with the crystallographic B-factors, indicating that the overall protein structure and dynamics as observed by x-ray crystallography is also captured in the
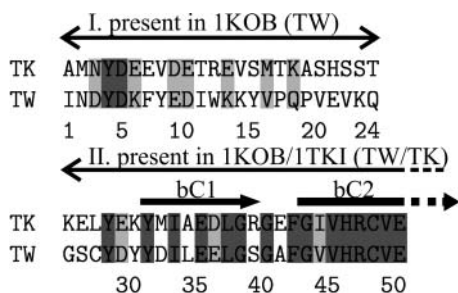
FIGURE 2 Sequence alignment of the N-terminal regions of titin kinase and twitchin kinase. Invariant and semiinvariant residues are highlighted with a dark shaded and light shaded background, respectively. The numbering refers to twitchin kinase.

simulation (data not shown). The only significant deviation from the x-ray structure was seen for the catalytic site residues. According to the crystal structure, Asp[127], the catalytic base, and Arg[129], both conserved residues of serine/threonine kinases, form a double salt bridge. At the nanosecond timescale of the free dynamics simulation, this salt bridge is reversibly broken and mostly substituted by a Glu[131]-Arg[129] salt bridge (Fig. 3). This catalytic site ''wobbling'' was not seen for the free MD simulation of twitchin kinase, where the homologous Asp[152]-Lys[154] salt bridge stayed intact.

Unfolding mechanism

Force-probe unfolding simulations have been carried out with pulling speeds from 0.004 Å/ps to 0.5 Å/ps; the slowest pulling simulation covered 22 ns. This timescale is four to six orders of magnitude faster than the time scale in vivo and of AFM experiments. To estimate the dependence of the unfolding forces and mechanism on the timescale of the FPMD simulations, they were carried out at varying velocities covering a range of nearly two orders of magnitude. Unfolding forces observed for different pulling velocities are shown in Fig. 4 *a*. As can be seen, these forces are nearly equal for the N- and C-termini, respectively, which shows that the above expectation, that pulling at both sides reduces friction, was indeed justified.

To a good approximation, the rupture force F_{max} depends on the pulling velocity according to

$$F_{max}(v) = \gamma v + \frac{k_B T}{L} \ln \frac{v}{k_0 \Delta L}, \qquad (5)$$

where γ is a friction coefficient, L the unfolding length of the protein, ΔL the scatter of the unfolding length L, and k_0 the

rate constant of spontaneous unfolding (Evans and Ritchie, 1997; Heymann and Grubmüller, 1999). Equation 5 describes a linear dependency of the rupture force on v, in Fig. 5 seen for $v > 0.05$ Å/ps, the friction-dominated regime, and a logarithmic dependency for $v \leq 0.05$ Å/ps, the thermally activated regime. Typically, FPMD does not allow for extrapolating to experimental timescales. Therefore, Heymann and Grubmüller (1999) have suggested using the spontaneous unfolding rate k_0 as additional experimental input. Unfortunately, this rate has not yet been measured for titin kinase, so that a prediction of rupture forces at the experimental timescale is not possible at present.

The rupture events observed in the FPMD simulations of the logarithmic regimes were compared with each other and found to be similar with respect to the main features, as described below. If not otherwise mentioned, the results of the 0.004 Å/ps simulation are therefore presented.

Unfolding dynamics are mainly governed by the rupture of the terminal anti-parallel β-sheets, in particular by the rupture of hydrogen bonds between the strands βC1, βC2, and βC3 at the N-terminus (*I*) and those between βC10, βC11, and βR1 at the C-terminus (*II*) (Fig. 5). The largest force is required for the C-terminal βC10-βR1 rupture, which is preceded by the βC11-βR1 rupture at lower force. At the N-terminus, rupture of the βC1-βC2 β-sheet is followed by the βC2-βC3 rupture. Another main rupture event is the loss of secondary structure of the inhibitory tail sequence αR2, which coincides with its detachment from the ATP binding groove (*III*).

As the only major difference of the unfolding pathways between slower and faster pulling simulations, we observed the sequence of events I–III (Fig. 5). The FPMD simulations with $v = 0.05$ Å/ps and $v = 0.004$ Å/ps shall serve as the most pronounced examples: At a velocity of 0.05 Å/ps,
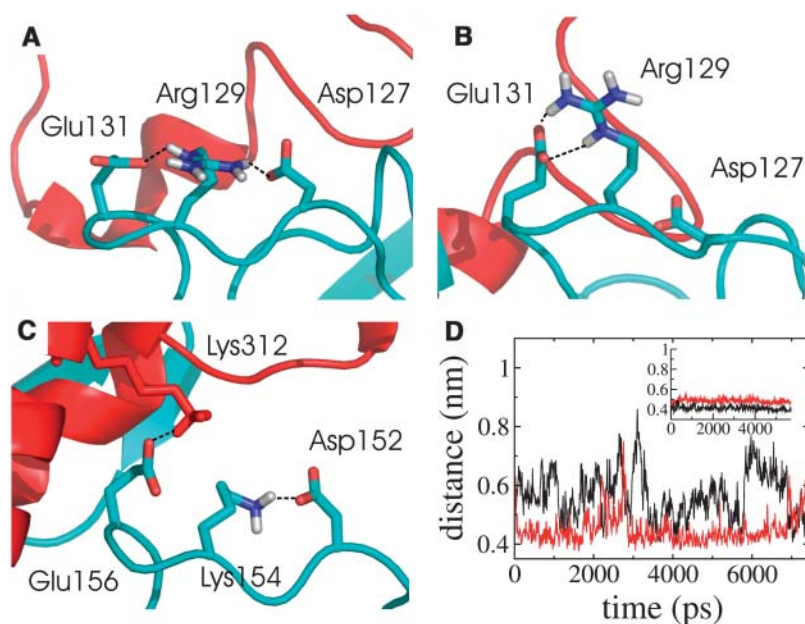

FIGURE 3 (*a–c*) Snapshots of titin kinase at 3.7 ns and 6.0 ns, and of twitchin kinase at 2.7ns. (*d*) Comparison of the side-chain fluctuations of the titin kinase (*main panel*) and twitchin kinase catalytic sites (*inset*). Center-of-mass distances between the side chains of Asp[127] and Arg[129] (*black*) and of Arg[129] and Glu[131] (*red*) of titin kinase are shown. The inset shows the respective distances between Asp[152] and Lys[154] (*black*) and Lys[154] and Glu[156] (*red*) of twitchin kinase.
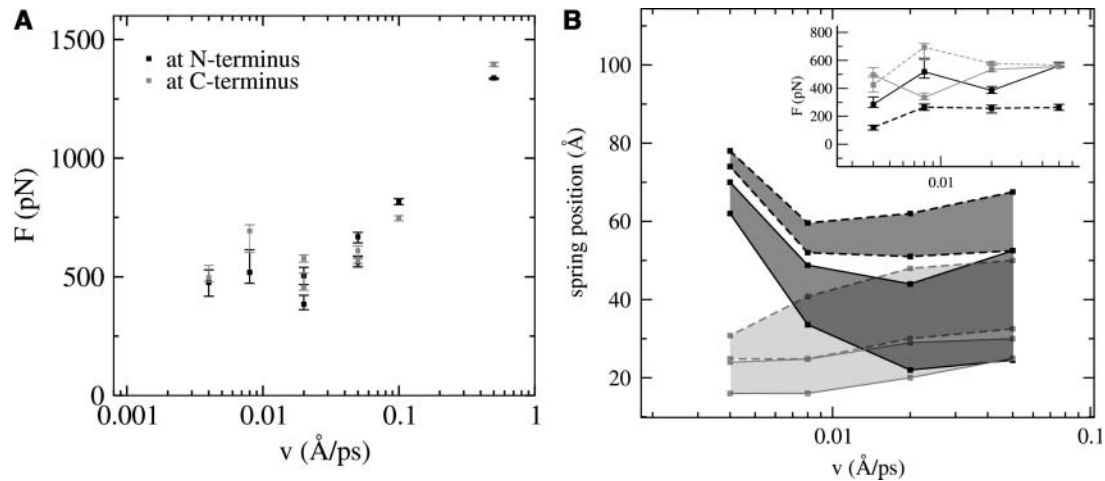
FIGURE 4 (*a*) Maximal rupture forces as a function of pulling velocity *v* for the N-terminus (*black*) and C-terminus (*red*). Error bars indicate the uncertainty in the maximal rupture force due to the choice of a Gaussian distribution width for smoothing (see Methods section). (*b*) Spring positions (dislocation with respect to the starting position) at which the first (*solid*) and final (*dashed*) rupture of two N-terminal (*black*) and two C-terminal (*gray*) β-sheets occur, as a function of the pulling velocity for the four slowest pulling simulations. The inset shows the maximal rupture force observed during the period of the four β-sheet ruptures.

N- and C-terminal β-sheet ruptures occur simultaneously after the spring positions have moved by ∼35 Å each. At the end of the simulation, αR2 has lost its secondary structure only partially and did not substantially dislocate from the ATP binding site between the small and big lobe. Instead, αR2-small lobe interactions are partially disrupted due to the dislocation of βC1 and βC2 at the time of N-terminal β-sheet rupture.

In contrast, during the FPMD simulation with $v = 0.004$ Å/ps, ruptures of the C-terminal β-sheet at a spring position of 15–30 Å clearly precede that of the N-terminal β-sheet (62–78 Å). As a consequence of the higher force resistance of the βC1-βC2 β-sheet relative to the βC10-βR1 β-sheet, αR2 leaves the active site before ruptures at the N-terminus. The force peak at a spring location of 42 Å can be attributed to the simultaneous rupture of interactions between αR2 and the small lobe, of which the β-sheet still is taking up its original conformation and hydrogen bond pattern.

In general, as shown in Fig. 4, a decrease in pulling velocity leads to a stabilization of the N-terminal β-sheet with respect to the C-terminal β-sheet. However, a similar tendency is not observed for the forces required for these ruptures (Fig. 4, *inset*). Here, the relative stabilities of β-sheet ruptures are not reflected by the rupture force but rupture time. Except from the terminal β-strands and the inhibitory tail, the protein secondary and tertiary structure keeps remarkably stable. After a dislocation of 92 Å of each spring, the titin kinase remains its native secondary structure fold for 50% of its residues, or for 64% of the residues not yet pulled out of the protein core.

Open-closure motion

For four FPMD simulations at low pulling velocity, principal components of the titin kinase dynamics have been calculated to characterize the main collective motions induced by the applied mechanical stress. The FPMD runs were used to calculate the covariance matrix of the protein backbone atoms, and after projection onto the largest eigenvectors, similar global domain motions were found for each of the four trajectories. In all cases, the eigenvector contributing mainly to the total protein motion (with a contribution of 76–86% to the total fluctuations) describes the movement of the
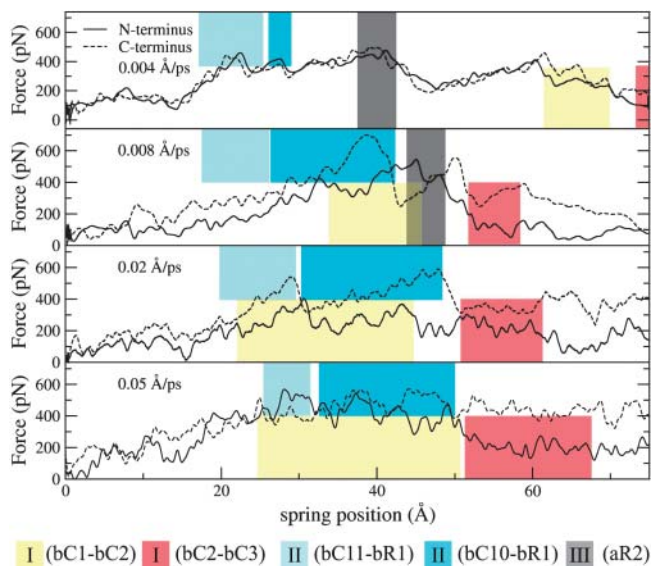

FIGURE 5 Force profiles and main rupture events for FPMD simulations of the low velocity regime. N-terminal ruptures (*I*) are shown in yellow and red, C-terminal ruptures (*II*) in light and dark cyan, and the αR2 rupture (*III*) in gray.

terminal protein sequences apart from each other, and, in this sense, is the trivial one. The more relevant second-largest eigenvector, with a contribution of 7–8%, describes an open-closure motion involving the active site (Fig. 6). During the 0.004 Å/ps simulation, e.g., the projection of the trajectory onto the second eigenvector (Fig. 6 a) decreases until a spring position of 60 Å is reached. Structural inspection (Fig. 6 b) shows that this drop describes an opening motion of the active site. The subsequent rupture of the N-terminal β-sheet then yields the main drop in force, leading to a closure motion of the small and big lobe. This relaxation of the strained protein conformation is reflected by a subsequent increase of the projection of the second eigenvector, and thereby restores the initial binding site geometry. The open-closure motion closely resembles the one observed also in the conformational transition from inactive to active states in other protein kinases like insulin receptor tyrosine kinase (Hubbard, 1997).

According to the domain analysis of the second eigenvector with DynDom (Hayward and Berendsen, 1998), the whole regulatory tail, including the αR1 and αR2 segments, moves collectively together with the small lobe (Fig. 6 b). Accordingly, α2 maintains its tight interactions to small lobe residues until rupture of those at a spring position of 44 Å, i.e., briefly before the closure motion sets in. In contrast to αR2, which at a spring position of 90 Å has moved to an RMSD of 40 Å, αR1 shows a deviation from its initial conformation by <5 Å. Thus, though moving in correlation with αR2, the total fluctuations of αR1 are significantly smaller. The two main hinge points for the open-closure motion are located at i), the big lobe regulatory tail interconnection N-terminal of αR1 (residues 272–273) and neighboring sequences, and ii), at residues 60–66 (small lobe) and residues 141–145 (big lobe), which is the only region at which the big and small lobes stay tightly aligned during force-induced unfolding (Fig. 6 b).

Comparison of the principal component analysis of all FPMD simulations shows that both the eigenvectors, which characterize the nature of the main collective motions, as well as the associated eigenvalues, which measure the associated amplitudes of these motions, are largely unchanged by the pulling velocity. The most pronounced change is seen for the first eigenvector, which contributes between 86% (v = 0.05 Å/ps) and 76% (v = 0.004 Å/ps) to the overall dynamics. This finding is in line with the observation that also the rupture forces drop only slightly below 0.005 Å/ps (Fig. 4 a) as expected for a low unfolding rate. Taken together, this indicates that the FPMD simulations presented here, even though restricted to nanoseconds, capture a relevant fraction of the conformational dynamics that are expected at the physiological and experimental timescales.

β-Sheet ruptures

Molecular dynamics simulation results

To elucidate the molecular origin of the pronounced and unexpected asymmetry in the stability of the two terminal β-sheets, we compared their hydrogen bond rupture pattern. Fig. 7 shows the hydrogen potential energy as a function of time for the ruptures at the N- and C-termini.

As can be seen, hydrogen bonds between the strands βC1 and βC2 rupture concurrently within a very short time interval, in response to a shearing force acting parallel to the β-strands in opposite directions (cf. the sketch and snapshots in Fig. 8). The strands slide along each other until they snap in again by forming a new set of hydrogen bonds. In sharp contrast, the β-strands at the C-terminus, oriented approximately vertically with respect to the pulling direction, rupture in a stepwise manner, resulting in a zipperlike opening of the β-sheet, and nonnative hydrogen bonds are not formed (Fig. 8). As already observed for the overall conformational motions, this pronounced contrast of concurrent versus sequential rupture of the β-sheets also is seen in all FPMD simulations. The sliding-snapping mechanism is only seen for pulling velocities that are slow enough to provide sufficient relaxation time for the transient
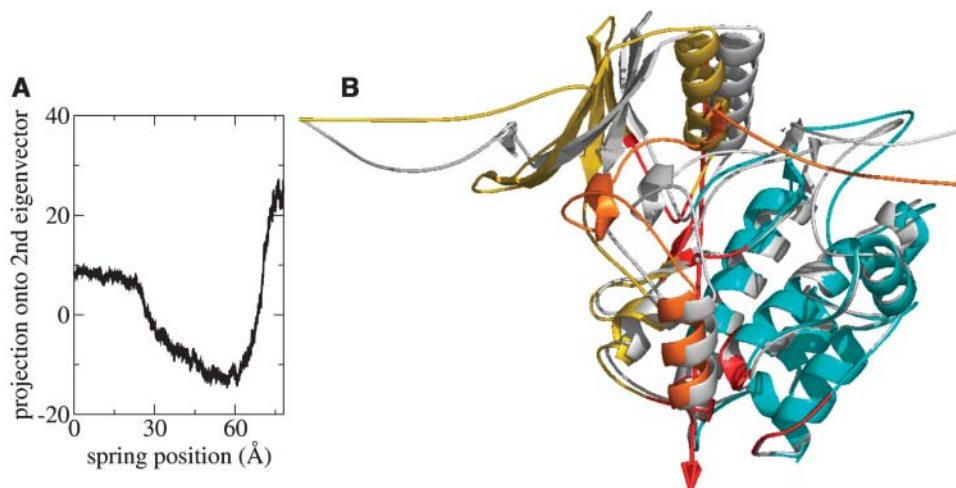

FIGURE 6 Open-closure motion of the small and big lobe during pulling. (a) Projection onto the second eigenvector as a function of simulation time. (b) Overlay of the extreme projections of the titin kinase motion on the second eigenvector (gray, closed conformation; colored, open conformation). The hinge axis between the two dynamic domains as determined with DynDom (Hayward and Berendsen, 1998) (cyan, big lobe; yellow and orange, small lobe and regulatory tail) is depicted as red arrow; hinge residues are shown in red.
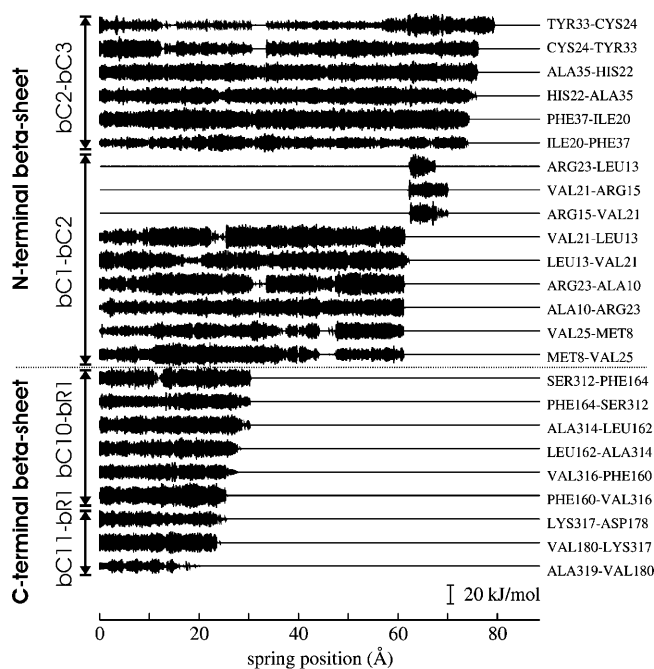
FIGURE 7 Hydrogen bond interactions at the terminal β-sheets. Shown are hydrogen bond strengths for each hydrogen bond between the β-strands as indicated. As can be seen, βC1-βC2 ruptures simultaneously, the other sheets sequentially. For simultaneous rupture, subsequent transient hydrogen bonds are seen.

β-hydrogen bonds to form (once for $v = 0.004$ Å/ps, twice for $v = 0.008$ Å/ps).

Assuming that the two β-sheet ruptures occur independently from each other, the order of ruptures can be used to characterize the relative mechanical stability of the respective β-sheets—the weaker β-sheet should rupture first. Indeed, the β-sheet in parallel to the pulling direction ruptures at higher loads, and thus is more force resistant, than the β-sheet vertical to the pulling direction (Fig. 4). This is not unexpected, since the concurrent rupture of N hydrogen bonds requires a higher force than a single bond rupture within a sequential rupture, as it has been shown previously (Lu et al., 1998; Lu and Schulten, 2000; Rohs et al., 1999; Brockwell et al., 2003).

Interestingly, this difference in stability vanishes for increasing pulling velocity (Fig. 4). Can the differential stabilities and their convergence at high pulling velocities be sufficiently and quantitatively explained by the different energy landscapes underlying the concurrent and sequential rupture mechanisms? How would one expect them to scale toward experimental pulling velocities? To answer these questions and to understand the underlying physics, we have performed force-probe Monte Carlo simulations.

Monte Carlo simulation results

As a simple model, we describe sequential and concurrent rupture by the one-dimensional energy profiles shown in Fig.

9 b. The average potential of a single hydrogen bond was set to −23 kJ/mol, the average value obtained for the relevant bonds from the MD simulations according to Eq. 4. For sequential rupture (Fig. 9 a, top), a stepwise increasing hydrogen bond potential was chosen (Fig. 9 b). A single rupture event involves the rupture of one hydrogen bond, and, therefore, leads to an increase in potential energy along the reaction coordinate $x_2 - x_1$ by −23 kJ/mol with a low activation barrier. Each rupture event of the concurrent rupture (Fig. 9 a, bottom), in contrast, involves an increase in hydrogen bond energy from negative values to 0 kJ/mol, as all hydrogen bonds rupture at each sliding event along x_1. For both types of rupture, the change along the reaction coordinate was set to 1 nm to equal the average increase of this distance observed in the MD simulations during a complete rupture. Taken together, the system moves within a two-dimensional energy landscape (Fig. 9 c).

In the FPMD simulations, β-sheet rupture is followed by a fast unfolding of the released peptide chain. To account for its elasticity in the Monte Carlo simulations, a wlc element was attached to each β-sheet. This element was modeled by allowing steps along each reaction coordinate after the respective hydrogen bond potential has been traversed ($x_1 > 1$ nm and $x_2 - x_1 > 1$ nm, respectively) on a wlc energy surface (Eq. 3) with a contour length of 2.5 nm.

Fig. 9 d shows the spring positions at which the first and last hydrogen ruptures of the β-sheets occur for varying spring velocities, which is to be compared to the MD results shown in Fig. 4 b. As expected, for low pulling velocities, the parallel occurs after the sequential rupture, with the two ruptures well separated from each other, in correspondence to the FPMD results. The trajectory of an FPMC run in this regime leads along the border of the energy profile of Fig. 9 c (first along $x_2 - x_1$ with $x_1 = 0$, then along x_1 with $x_2 - x_1 = 0$).

The increase of the spring positions with pulling velocity that was seen in the MD simulations is also observed here. In particular, for large pulling velocities, the rupture processes take longer, in qualitative agreement with the MD simulations (Fig. 4 b). Below $v = 50 \times 10^{-5}$ nm/step, the two different positions at which the two β-sheets rupture do not change considerably, which suggests that this sequence of events, as seen in the MD simulations, is likely to be observed also at physiological and experimental timescales. For large velocities, the spring positions of the final C-terminal rupture and the starting N-terminal rupture approach each other and finally overlap. The simultaneous rupture of both β-sheets corresponds to a trajectory that diagonally traverses the energy surface of Fig. 9 c. The crossover takes place when the velocity, at which the spring is dislocated at each step, exceeds the average step size, i.e., when Stokes friction sets in, which in the MC simulations is implicitly described via the diffusion coefficient that is set by the ratio between squared positional step size and the time step. Above this point, unfolding can not keep up with the fast movement of
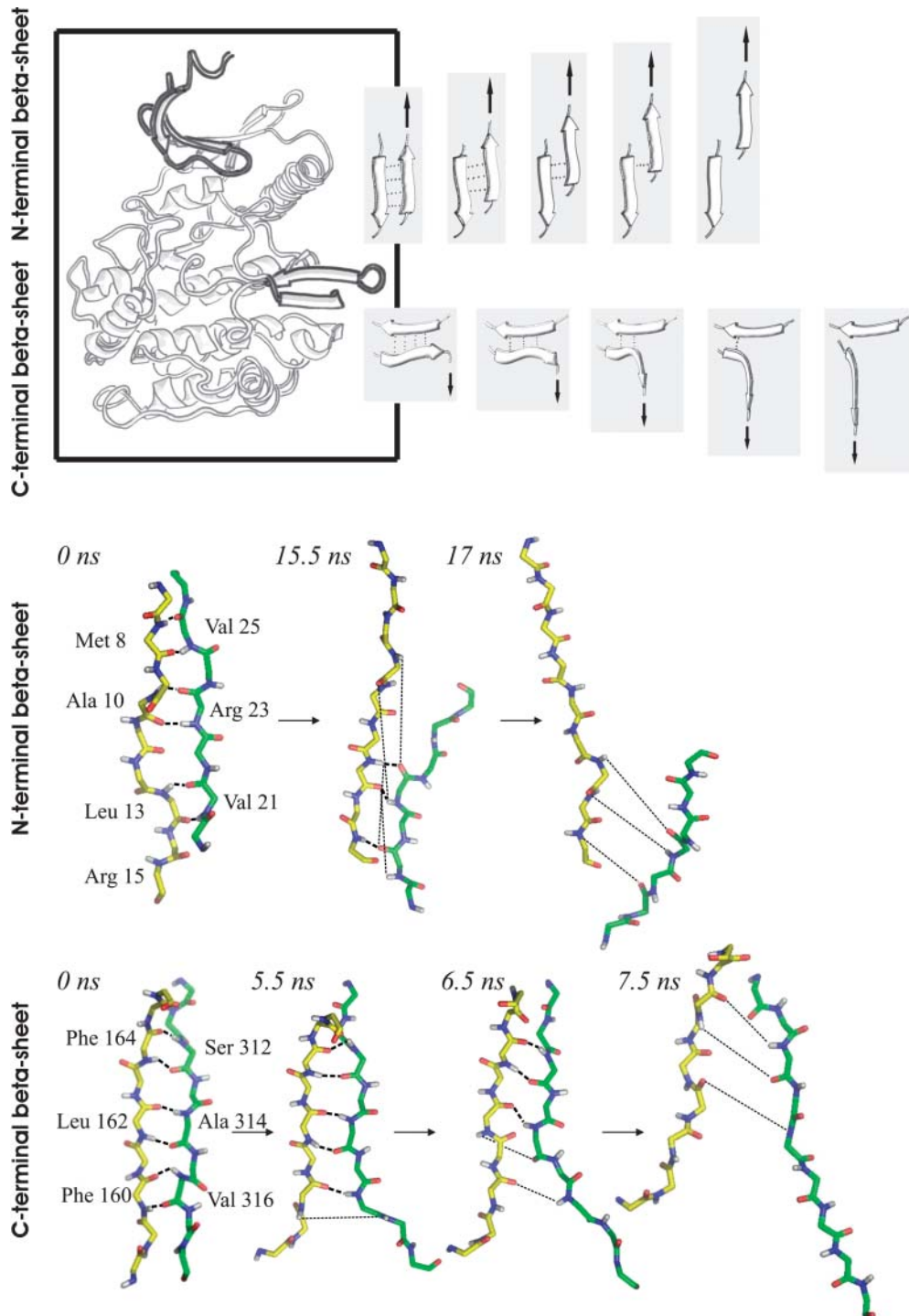
FIGURE 8 Differences of hydrogen bond rupture patterns for the two terminal β-sheets. (*Upper panel*) Sketch of the sequence of ruptures at the N-terminus (*top*) and the C-terminus (*bottom*). (*Lower panel*) Snapshots of the N-terminal βC1 and βC2 (*yellow* and *green*, respectively, *top*); snapshots of the C-terminal βC10 and βR1 (*yellow* and *green*, respectively, *bottom*). Hydrogen bonds are drawn as dashed (intact) and dotted (ruptures briefly before) dashed lines.

the spring. In agreement with the MD simulation results (Fig. 4), the crossover occurs within one order of magnitude of pulling velocities.

A striking difference between the dynamics of concurrent and sequential rupture was found in the individual rupture events as quantified by the steepness of the potential energy increase with time. In the FPMC simulations, the dislocation of the spring during which a rupture event takes place was two orders of magnitudes larger for the sequential as compared to the concurrent rupture. In other words, hydrogen bonds rupture within a significantly longer time interval in a sequential rather than in a concurrent fashion.

Is this differential behavior as found for the simple two-dimensional model also in agreement with the molecular dynamics simulations? We studied the rupture dynamics of the β-sheet hydrogen bonds during the FPMD simulations
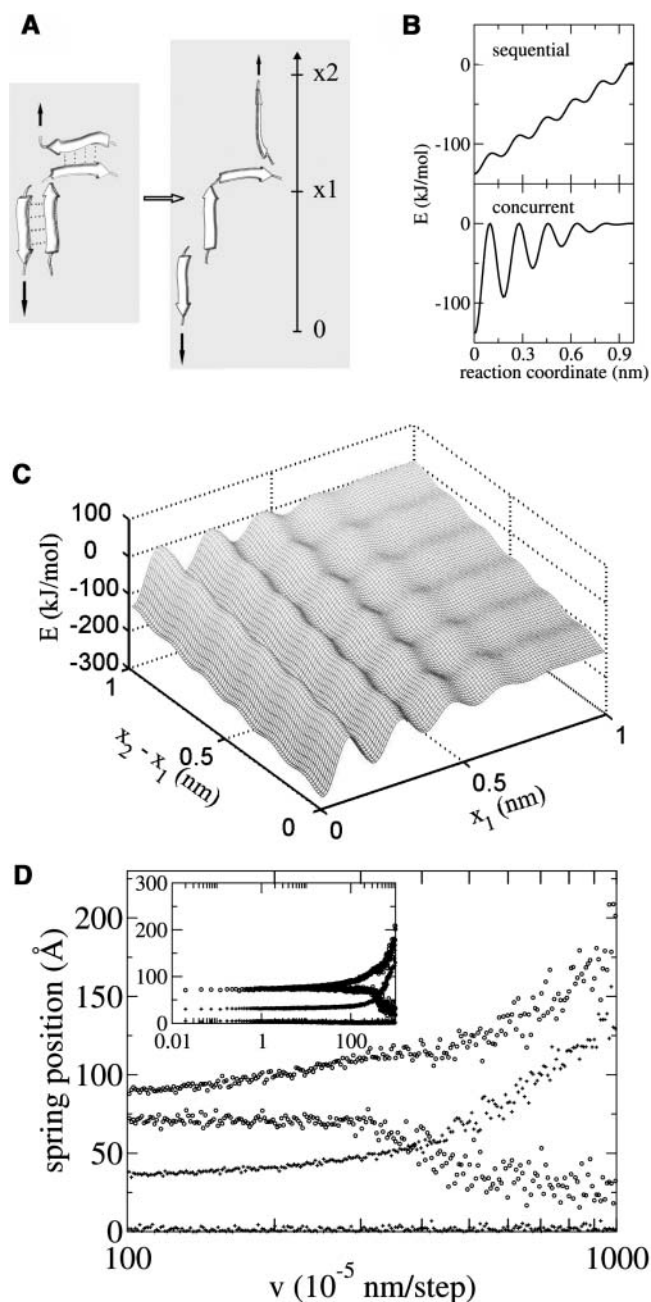
FIGURE 9 Force-probe Monte Carlo simulations with model energy landscapes. (*a*) Sketch of the model system: two attached β-sheets rupturing concurrently (*top*) and sequentially (*bottom*). (*b*) Assumed one-dimensional energy profiles for the sequential and concurrent rupture of a β-sheet with six hydrogen bonds. (*c*) Combined hydrogen bond potential energy surface $G(x_1, x_2 - x_1)$. Here, x_1 is the reaction coordinate of the sequential, $x_2 - x_1$ that of the concurrent rupture, respectively, combining the profiles of *b*. (*d*) Spring positions at which the first (*lower curve*) and final rupture (*upper curve*) of the β-sheets occur as a function of the pulling velocity for the concurrent ($\bigcirc$) and the sequential ($+$) rupture. The inset shows data for a larger velocity range.

by examining the potential energy of individual hydrogen bonds. The interval, in which a hydrogen bond potential drops from the value of 23 kJ/mol on average to 0 kJ/mol, was assessed by fitting a properly chosen function to the hydrogen bond energy trace (see Methods section and Fig. 10). As can be seen, hydrogen bonds that rupture concurrently show a smaller width a_0 of the potential decrease than those that rupture sequentially.

A more sudden rupture of a sheet under longitudinal force indeed is expected, since a weakening of the hydrogen bonds between the strands leads to the complete loss of interactions and a large sliding movement until the strands snap in again. At the time of single hydrogen bond rupture of a series of sequential ruptures as seen at the C-terminus, instead, the remaining interactions keep the residues that are breaking apart in closer proximity, allowing for a slow hydrogen bond potential decay. The width a_0 decreases with decreasing pulling velocity for the same reason that causes the decrease of maximal rupture force (Fig. 4); with a lower loading rate, a rupture becomes likely already at lower loads due to thermal activation. In summary, the difference in the abruptness of the hydrogen bond potential decay between concurrent and sequential rupture seen in the Monte Carlo simulations was also found in the corresponding FPMD simulations, thus providing further support that our simple two-dimensional model captures the underlying physics of the rupture process.

Release of autoinhibition

The titin kinase regulatory tail (residues 275–321), particularly the αR2 helix (residues 296–301), tightly binds to the active site via multiple hydrogen bonds and van der Waals contacts. If not noted otherwise, we subsequently report the results for the simulations with a pulling velocity of 0.004 Å/ps. Similar results have been obtained for the other simulations in the low velocity regime.

As can be seen in Fig. 11, van der Waals contacts rupture simultaneously at a spring position of 44 Å. These ruptures are the main trigger for αR2 release from the active site groove. Together with the rupture of the intrahelical hydrogen bonds of αR2, this event gives rise to a force peak. Interactions of αR2 to the active site also include those to side chains of residues known to be involved in ATP binding (Lys[36], Glu[51], Asp[87], and Glu[147], data not shown). In all simulations, the inhibition of residues Glu[51] and Glu[147] is removed before the rupture of van der Waals contacts to the small lobe; the Glu[51]-Ala[304] hydrogen bond ruptures at a spring position of 36 Å, the Glu[147]-Gly[303] hydrogen bond ruptures at 30 Å, respectively. An early rupture of the initial Lys[36]-Gly[302] hydrogen bond at 10 Å is followed by the formation of a Lys[36]-Ile[299] hydrogen bond, which ruptures at 45 Å, i.e., immediately after the main breakage of van der Waals contacts to the small lobe. Asp[87] forms a transient hydrogen bond to regulatory tail Ser[295], which finally breaks at a spring position of 42 Å.
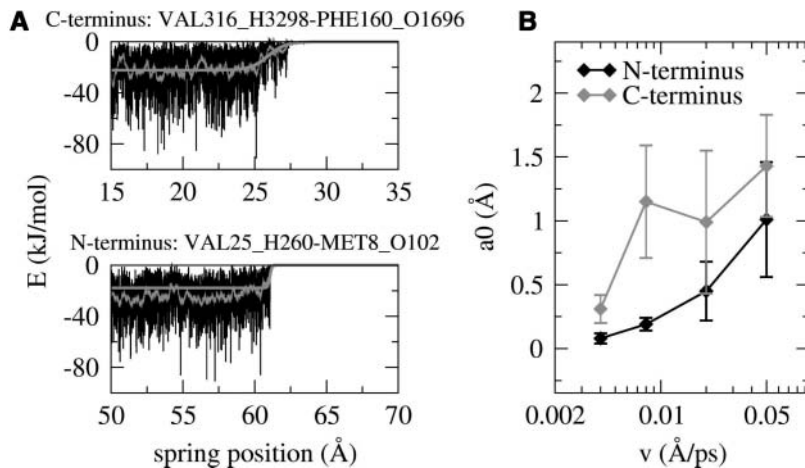
FIGURE 10 Difference between fast and slow hydrogen bond ruptures. (*a*) Hydrogen bond potentials (*black*), running average over 50 ps and fit to the running average with a logistic function (*shaded*, see Methods section). Shown are two representative hydrogen bond ruptures at the N- and C-termini, respectively. (*b*) Width a_0 of the fitting function as a measure for the abruptness of the rupture process. Values are averaged over the hydrogen bonds of the sheet; error bars give the variance among them.

In summary, together with the detachment of the hydrophobic contacts between the regulatory tail and the small lobe, autoinhibition of the ATP binding residues is removed. Despite the variability of side-chain conformations, all low velocity FPMD simulations share the relevant specific residue-residue interactions, although the detailed sequence of ruptures may differ, due to variations of the spring position at rupture by ± 20 Å.

Is the structure of the active site after removal of the autoinhibitory tail sufficiently intact for kinase activity? To answer this question, the geometry of the active site was characterized by monitoring the distances between C_α atoms of the catalytic and ATP binding residues during the FPMD simulation (Fig. 12 *a*). As can be seen, all distances stay close to the distances seen in the titin kinase crystal structure (Mayans et al., 1998), as well as the crystal structures of its homologs twitchin kinase (Kobe et al., 1996) and extracel-

lular regulated kinase (ERK-2) (Zhang et al., 1994). The only exception is the distance between Lys[36] and Asp[127], which increases by ~ 2 Å. Further deviations from the crystal structure are transient, e.g., for Lys[36]-Asp[127] at 75 Å, and disappear during subsequent conformational relaxation, which takes place after the stress is reduced. We note that these transient deviations are smaller for slow pulling velocities, which suggests that they may be absent at physiological timescales. These results suggest that the active site integrity, though temporarily perturbed, is maintained to a sufficient extent to allow kinase activity. Since Tyr[170] remains with its $4'$ hydroxyl group oriented toward the catalytic base Asp[127], the semiopened catalytic cleft raises the possibility of an intramolecular autophosphorylation upon ATP binding.

The Gly-rich loop (residues 14–19), located in the small lobe between the β-strands βC1 and βC2, plays a role in accommodating ATP in the active site groove (Knighton et al., 1991; Bossemeyer, 1994). This loop remains stable upon mechanical relieve of autoinhibition, but does not remain close to the active site, when the small lobe unravels. As shown in Fig. 12 *b*, it is rather pulled apart as soon as the βC1-βC2 sheet ruptures at a spring position of ~ 60 Å. As a consequence of the N-terminal β-sheet destabilization with increasing pulling velocity (Fig. 4), the Gly-rich loop is removed from its active site location before the release of autoinhibition for high pulling velocities, whereas for small velocities such as 0.004 Å/ps, release occurs from an intact N-terminal β-sheet including the Gly-rich loop.

Comparison to twitchin kinase unfolding

During the 6 ns FPMD simulation, twitchin kinase shows little conformational changes in the protein core, but mainly separates from the N-terminal random coil (residues 1–24), giving rise to a force maximum of 430 ± 21 pN at 2.6 ns (Fig. 13). This force maximum can be attributed to ruptures of mainly four polar interactions, namely Asp[5]-Ser[109], Asp[5]-Lys[163], Gln[18]-Leu[91], and Gln[18]-His[92]. All of the involved
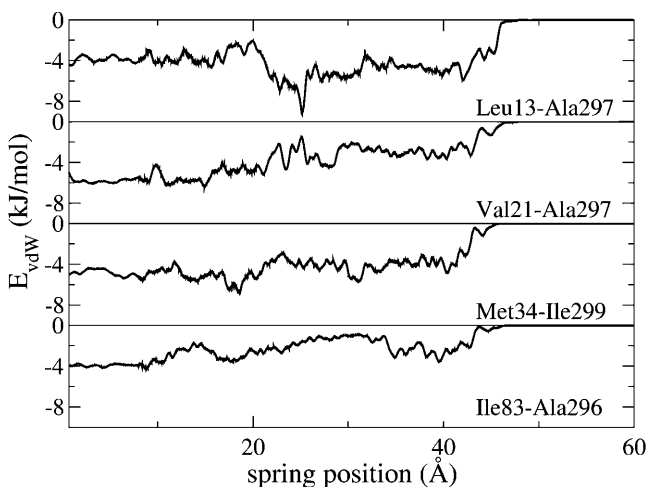

FIGURE 11 One-step rupture of the inhibitory tail from the small lobe. The van der Waals interaction energy for residue pairs of the small lobe (1–83) and αR2 (296–301), smoothed by Gaussian filtering with a band width of 100 ps, is shown.
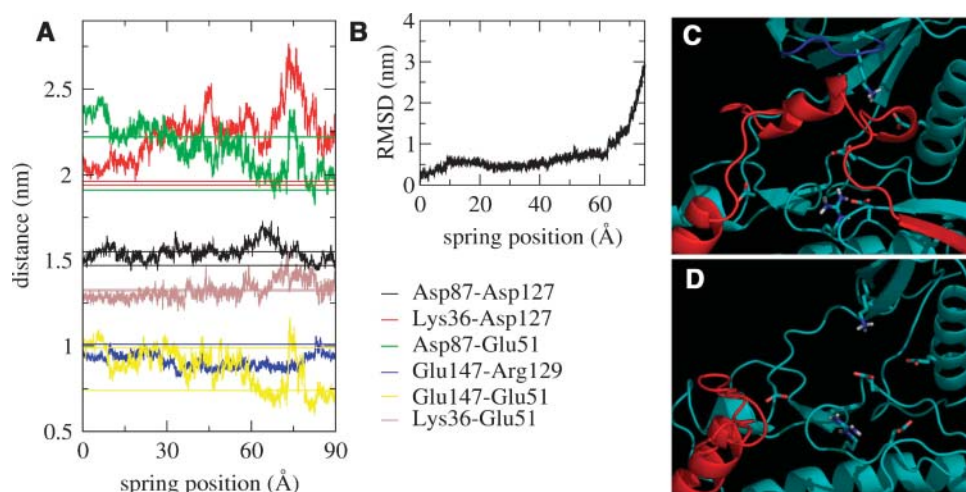
FIGURE 12 Integrity of the active site. (a) C_α-distances of ATP binding residues. Straight lines are the equivalent distances in twitchin kinase (Kobe et al., 1996) and extracellular regulated kinase (ERK-2) (Zhang et al., 1994). (b) Displacement of the Gly-rich loop shown as root-mean square deviation of residues 14–19 from the starting structure. (c and d) Snapshots of the active site before (0 ns) and after (22 ns) the release of autoinhibition. ATP binding and catalytic residues are shown as sticks, the regulatory tail in red, and the Gly-rich loop in blue.

residues are strictly conserved in titin kinase, except Lys[18], which is converted to functionally equivalent Gln (Fig. 2). It can be concluded that a similar force pattern can be expected for the respective unfolding of a titin kinase domain including the additional sequence.

To estimate the error in the protein conformational changes due to the lack of the N-terminal coil in the titin kinase structure, the dislocation of the terminal β-strands during pulling was compared to the one observed during twitchin kinase pulling (Fig. 13). In both kinases, dislocation of the C-terminal βR1 strand occurs sooner and to a larger extent than dislocation of the N-terminus. Thus the conformational changes of the β-sheets are not significantly affected by the presence of the additional N-terminal sequence.
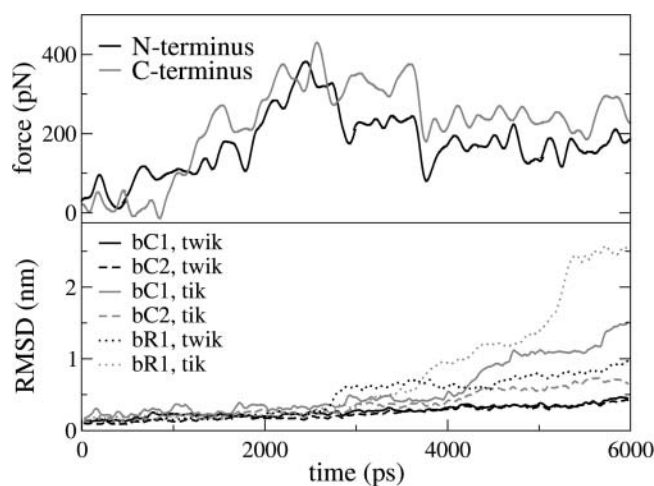

FIGURE 13 (Upper panel) Force profile as obtained from the twitchin kinase pulling simulation with 0.008 Å/ps velocity after Gaussian filtering. (Lower panel) Comparison of the terminal β-sheet dislocation between twitchin kinase and titin kinase during the first 6 ns of the 0.008 Å/ps pulling simulation.

The initial pulling direction, defined as the vector connecting the twitchin kinase termini, differs from that chosen for titin kinase unfolding by 100°. With regard to the anisotropy of the mechanical stability of β-sheets, the question arises whether the fact that the N-terminal coil is missing in the titin kinase structure affects the FPMD results discussed here. Comparison with the twitchin kinase simulation allows this uncertainty to be addressed. As can be seen in Fig. 14, detachment of the N-terminal coil of twitchin kinase induces an overall rotation of the whole protein, such that the pulling direction becomes similar to that of titin kinase. Therefore, we consider artifacts from the initial difference in the pulling directions unlikely.

DISCUSSION AND CONCLUSION

We have carried out force-probe simulations of titin kinase to test the hypothesis that this titin domain is a force sensor that can be activated by mechanical stress. Our results suggest that mechanical strain on this domain leads to an ordered sequence of conformational changes that result in an open conformation of the catalytic cleft without unfolding of the catalytic core of the enzyme. Titin kinase is the only kinase among Ca^{2+}/calmodulin-activated kinases, of which the catalytic site Lys is substituted by Arg (Mayans et al., 1998). The wobbling behavior of the titin kinase catalytic site as observed during the free MD simulation can be partially ascribed to the larger size of Arg compared to Lys, and its higher potency to form multiple salt bridges. Furthermore, in contrast to titin kinase, Glu[156] of twitchin kinase forms a salt bridge to Lys[312], a residue of the inhibitory tail, and thereby is directed away from Lys[154]. These findings may point to a role of the conserved Glu in influencing the catalytic base activity of Asp[127] in titin kinase, in addition to its participation in ATP binding, as generally assumed for serine/threonine kinases (Bossemeyer et al., 1993).
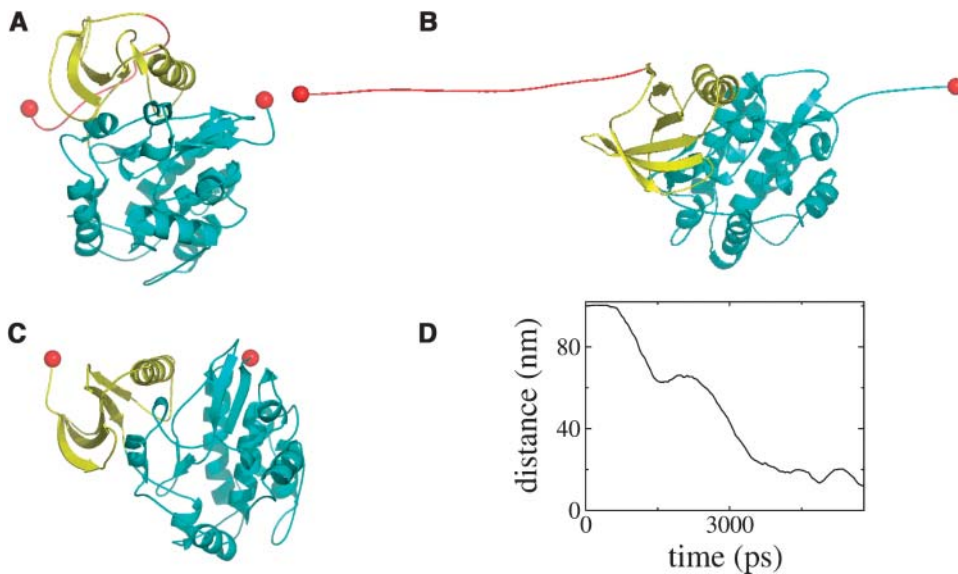
FIGURE 14 Comparison of the pulling geometry between twitchin kinase and titin kinase. (*a* and *b*) Snapshots of the twitchin kinase pulling simulation at 0 ns and 6 ns. (*c*) Titin kinase starting structure. In *a*–*c*, the big lobe is shown in cyan, the small lobe in yellow, and the pulled C_α-atoms as spheres in red. (*d*) Angle between the force vector during the twitchin kinase pulling simulation and the initial force vector for titin kinase pulling simulation.

FPMD simulations of protein unfolding face the problem of requiring a box length longer than the protein unfolding length, thereby, with respect to conventional MD simulations, necessarily including an amount of solvent molecules that is computationally impractical. Elongating spheres or repeated box enlargement during the simulation have been applied to tackle this problem (Lu and Schulten, 2000; Best et al., 2001). Here, cutting terminal protein segments and accounting for their elasticity by adjusting the spring constant proved to be an easy and efficient method to reduce the box length in pulling direction.

Information on the mechanical function of a protein can be obtained from its response to force. A number of proteins, those that in vivo are subjected to force (titin Ig/Fn3 domains) as well as those that are not, have been investigated by pulling experiments (AFM and optical tweezers) and MD. In AFM experiments, β-sandwich proteins such as titin Ig and Fn3 have been found to unfold at significantly higher forces (130–300 pN (Rief et al., 1997, 1998; Li and Fernandez, 2003) for I-band Ig, 180 pN in average for central A-band Fn3 (Rief et al., 1998)) than the nonmechanical protein barnase (50–100 pN (Best et al., 2001)) and the cytoskeleton component spectrin (25–35 pN (Rief et al., 1999)). By comparing those findings with our FPMD results, the force resistance of titin kinase can be classified. The maximal rupture force of 670 pN as found for titin kinase unfolding at 0.05 Å/ps (corresponding to 0.1 Å/ps if one terminus is fixed and the other one pulled) lies below the unfolding forces of Ig27 domains (1350 pN (Lu and Schulten, 2000)) and Ig1 domains (1000 pN (Gao et al., 2002)) found for pulling one terminus with 0.1 Å/ps (Fig. 4). Fn3 domains have been shown to unfold at forces of 1000–1300 pN at pulling velocities of 0.01 Å/ps (Gao et al., 2003), and therefore are another example of titin domains that are

more force resistant than titin kinase (500 pN at 0.004 Å/ps). Barnase, instead, was found to unfold at lower forces (270 pN at 0.01 Å/ps (Best et al., 2001)) than titin kinase (610 pN at 0.008 Å/ps). Thus, titin kinase takes up a medium position, ranking below the mechanically most stable β-sandwich proteins Ig and Fn3 and above those containing α-helical secondary structure. This is exactly what is to be expected for a force sensor reporting large mechanical stress that may unfold Ig domains of titin.

Our FPMD results show that the largest forces are required to rupture interstrand hydrogen bonds. Therefore, the terminal β-sheets can be considered as the mechanical elements mainly responsible for the remarkable force resistance. With a typical kinase fold, titin kinase is at first sight not expected to have specifically evolved for the sake of force resistance. From this point of view, the force resistance along with the significant catalytic site stability is unexpected.

For slow pulling velocities ($\leq$0.05 Å/ps), the N-terminal βC1-βC2 sheet is significantly more stable than the C-terminal βR1-βC10 sheet. As discussed below, the order of their rupture, i.e., their relative force resistance, is the main feature of the force-induced activation mechanism. The precedence of the C-terminal sequential over the N-terminal concurrent rupture might be attributed to the orientation of the β-sheets. To get quantitative insight into the physics of this mechanism and the resulting differential stabilities, we have considered a two-dimensional model of the rupture of both terminal β-sheets, for which we have carried out FPMC simulations. The FPMC simulations yield a picture in quantitative agreement with the β-sheet rupture events observed during the FPMD simulations: At pulling velocities well below the friction-dominated regime, the rupture of the β-sheet oriented vertically to the pulling direction is clearly

favored over the one oriented in parallel. At high velocities, however, the force resistances approach each other, resulting in a rupture of the two β-sheets at similar spring positions. The good agreement of the FPMC results with those observed in the FPMD simulations of the full titin kinase indicates that our simplistic two-dimensional model, although it neglects other protein domains and solvation, captures the main physics underlying the differential force resistance of differently oriented β-sheets.

In particular, the differential force resistance of the terminal β-sheets is attributed to their differential orientation to force and consequential unfolding mechanism. Whereas the N-terminal sheet can rotate such that its strands are positioned in parallel to the pulling direction, βC1 of the C-terminal β-sheet lies fixed upon the kinase domain and prescribes a vertical orientation toward the pulling direction. The parallel (in contrast to the vertical) orientation stabilizes the N-terminal over the C-terminal β-sheet. It is the depleting effect of the large spring potential onto the potential energy surface that weakens the N-terminal with respect to the C-terminal β-sheet at high pulling velocities.

We conclude that the catalytic site of the titin kinase is protected by an N-terminal β-sheet that is aligned in parallel to force, whereas the C-terminal regulatory tail achieves a high force sensitivity by aligning the C-terminal β-sheet vertical to force. Hence, by means of pulling geometry, the active site is protected against disintegration on the N-terminal site, and the release of autoinhibition is facilitated on the C-terminal site. The FPMC simulations suggest that at experimental and physiological timescales, i.e., for pulling velocities four to five orders of magnitude below the crossover regime, the difference in β-sheet stabilities is still present. Thus, the force-induced activation mechanism as described here should hold also at these slow time scales.

Studies on ubiquitin (Carrion-Vazquez et al., 2003) and a lipoyl domain of pyruvate dehydrogenase, E2lip3 (Brockwell et al., 2003), have recently yielded similar examples showing that beyond the number and nature of intrastrand hydrogen bonds, their relative orientation toward the pulling direction defines the stability of a β-sheet. The authors conclude that the same protein can exhibit different levels of force resistance depending on the pulling direction, thereby being easily unfoldable only under specific circumstances. Here, a different orientation of β-sheets of otherwise similar topology leads to a difference in mechanical domain stabilities within the same protein. The differential mechanical stability is required for the mechanical function. This finding demonstrates the importance of the dependency of the force resistance on the pathway when elucidating the unfolding mechanism.

In addition to the autoinhibition of the active site by the regulatory tail in the crystal structure, the catalytic base Asp[127] is blocked by Tyr[170], located at the P + 1 loop, via a hydrogen bond to its carboxylate group. It is assumed that phosphorylation of Tyr[170] removes this blockage and thus is required for titin kinase activation (Mayans et al., 1998). Although in FPMD simulations of high pulling velocity transient rupture of this interaction is observed at spring positions ranging from 36 Å to 40 Å, it is fully maintained during the 0.004 Å/ps simulation. Hence, the FPMD results do not suggest a force-induced release of the Asp[127] blockage.

Release of autoinhibition by αR2 dislocation leads to a structure of a principally intact kinase active site. Even at the final extension of 220 Å, the catalytic site integrity is striking, except that the Gly-rich loop, positioned above the ATP binding pocket and at the N-terminal β-sheet, is largely dislocated. However, a continuation of the trend toward N-terminal β-sheet stabilization with further lowering of the pulling velocity can be assumed. We speculate that at low velocities that are computationally not yet within reach, the autoregulatory tail vacates the active site before the displacement of the Gly-rich loop together with the N-terminal β-strand. Binding of Mg^{2+}/ATP to the exposed substrate binding cleft is likely to provide further stabilizing interactions for the ATP-binding lobe. Even after breakage of both terminal β-sheets and removal of the autoinhibitory tail, the secondary and tertiary structure of the kinase core remains remarkably intact. This is exactly what must be expected in light of the idea that the titin kinase is a force sensor activated by mechanical stress.

Remarkably, other domains behave quite differently. The Ig domains, for example, spontaneously disintegrate after rupture of β-sheets that are quite similar to those of the titin kinase (Lu et al., 1998; Lu and Schulten, 2000). Thus, the stability of the kinase core and, in particular, the active site, is quite an unusual feature, which adds considerable weight to our results in favor of the force sensor hypothesis. The conformation of the regulatory domain under mechanical activation, with αR2 and βR1 unfolded and an open ATP-biding site, is exactly the conformation found recently to bind tightly to the titin kinase associated signalsome (A. Yakovenko, S. Lange, E. Rostkova, J. Kristensen, B. Brandmeier, E. Ehler, S. M. Hughes, and M. Gautel, unpublished). This complex is involved in mechanically modulated regulation of protein turnover and gene transcription in muscle. We therefore propose that this postulated semiopen conformation can indeed be induced mechanically and thus can provide direct feedback of mechanical stress to the kinase signaling pathway.

In summary, the results presented here strongly support the assumption of a force-induced kinase activation. The hypothesis that titin kinase plays the role of a force sensor remains to be tested experimentally. Single-molecule experiments, in which the measured forces can be compared to those found in our simulations, are under way.

REFERENCES

Berendsen, H. J. C., J. P. M. Postma, W. F. van Gunsteren, and J. Hermans. 1981. Interaction model for water in relation to protein hydration. D. Reidel Publishing Company, Dordrecht, The Netherlands.

Berendsen, H. J. C., J. P. M. Postma, W. F. van Gunsteren, A. D. Nola, and J. R. Haak. 1984. Molecular dynamics with coupling to an external bath. *J. Chem. Phys.* 81:3684–3690.

Best, R. B., B. Li, A. Steward, V. Daggett, and J. Clarke. 2001. Can nonmechanical proteins withstand force? Stretching barnase by atomic force microscopy and molecular dynamics simulation. *Biophys. J.* 81:2344–2356.

Bossemeyer, D. 1994. The glycine-rich sequence of protein kinases—a multifunctional element. *Trends Biochem. Sci.* 19:201–205.

Bossemeyer, D., R. A. Engh, V. Kinzel, H. Postngl, and R. Huber. 1993. Phosphotransferase and substrate binding mechanism of the cAMP-dependent protein kinase catalytic subunit from porcine heart as deduced from the 2.0 Å structure of the complex with Mn^{2+} adenylyl imidodiphosphate and inhibitor peptide PKI(5–24). *EMBO J.* 12:849–859.

Brockwell, D. J., E. Paci, R. C. Zinober, G. S. Beddard, P. D. Olmsted, D. A. Smith, R. N. Perham, and S. E. Radford. 2003. Pulling geometry defines the mechanical resistance of a β-sheet protein. *Nat. Struct. Biol.* 10:731–737.

Carrion-Vazquez, M., H. B. Li, H. Lu, P. E. Marszalek, A. F. Oberhauser, and J. M. Fernandez. 2003. The mechanical stability of ubiquitin is linkage dependent. *Nat. Struct. Biol.* 10:738–743.

Centner, T., J. Yano, E. Kimura, A. S. McElhinny, K. Pelin, C. C. Witt, M. L. Bang, K. Trombitas, H. Granzier, C. C. Gregorio, H. Sorimachi, and S. Labeit. 2001. Identification of muscle specific ring finger proteins as potential regulators of the titin kinase domain. *J. Mol. Biol.* 306:717–726.

Darden, T., D. York, and L. Pedersen. 1993. Particle mesh Ewald—an $N \log(N)$ method for Ewald sums in large systems. *J. Chem. Phys.* 98:10089–10092.

DeLano, W. L. 2001. PyMOL Manual. DeLano Scientific, San Carlos, CA. http://www.delanoscientific.com.

Espinosa, E., E. Molins, and C. Lecomte. 1998. Hydrogen bond strengths revealed by topological analyses of experimentally observed electron densities. *Chem. Phys. Lett.* 285:170–173.

Evans, E., and K. Ritchie. 1997. Dynamic strength of molecular adhesion bonds. *Biophys. J.* 72:1541–1555.

Fowler, S. B., R. B. Best, J. L. T. Herrera, T. J. Rutherford, A. Steward, E. Paci, M. Karplus, and J. Clarke. 2002. Mechanical unfolding of a titin Ig domain: structure of unfolding intermediate revealed by combining AFM, molecular dynamics simulations, NMR and protein engineering. *J. Mol. Biol.* 322:841–849.

Gao, M., D. Craig, O. Lequin, I. D. Campbell, V. Vogel, and K. Schulten. 2003. Structure and functional significance of mechanically unfolded fibronectin type III_1 intermediates. *Proc. Natl. Acad. Sci. USA.* 100:14784–14789.

Gao, M., H. Lu, and K. Schulten. 2002. Unfolding of titin domains studied by molecular dynamics simulations. *J. Muscle Res. Cell Motil.* 23:513–521.

Gotthardt, M., R. E. Hammer, N. Hübner, J. Monti, C. C. Witt, M. McNabb, J. A. Richardson, H. Granzier, S. Labeit, and J. Herz. 2003. Conditional expression of mutant M-line titins results in cardiomyopathy with altered sarcomere structure. *J. Biol. Chem.* 278:6059–6065.

Grubmüller, H., B. Heymann, and P. Tavan. 1996. Ligand binding: molecular mechanics calculation of the streptavidin-biotin rupture force. *Science.* 271:997–999.

Hayward, S., and H. J. C. Berendsen. 1998. Systematic analysis of domain motions in proteins from conformational change: new results on citrate synthase and T4 lysozyme. *Proteins.* 30:144–154.

Hess, B., H. Bekker, H. J. C. Berendsen, and J. G. E. M. Fraaije. 1997. Lincs: a linear constraint solver for molecular simulations. *J. Comput. Chem.* 18:1463–1472.

Heymann, B., and H. Grubmüller. 1999. AN02/DNP-hapten unbinding forces studied by molecular dynamics atomic force microscopy simulations. *Chem. Phys. Lett.* 303:1–9.

Hubbard, S. R. 1997. Crystal structure of the activated insulin receptor tyrosine kinase in complex with peptide substrate and ATP analog. *EMBO J.* 16:5572–5581.

Izrailev, S., S. Stepaniants, M. Balsera, Y. Oono, and K. Schulten. 1997. Molecular dynamics study of unbinding of the avidin-biotin complex. *Biophys. J.* 72:1568–1581.

Isralewitz, B., M. Gao, and K. Schulten. 2001. Steered molecular dynamics and mechanical functions of proteins. *Curr. Opin. Struct. Biol.* 11:224–230.

Kellermayer, M. S. Z., S. B. Smith, H. L. Granzier, and C. Bustamante. 1997. Folding-unfolding transitions in single titin molecules characterized with laser tweezers. *Science.* 276:1112–1116.

Knighton, D. R., J. H. Zheng, L. F. Teneyck, V. A. Ashford, N.-H. Xuong, S. S. Taylor, and J. M. Sowadski. 1991. Crystal structure of the catalytic subunit of cyclic adenosine-monophosphate dependent protein-kinase. *Science.* 253:407–414.

Kobe, B., J. Heiherhorst, S. C. Feil, M. W. Parker, G. M. Benian, K. R. Weiss, and B. E. Kemp. 1996. Giant protein kinases: domain interactions and structural basis of autoregulation. *EMBO J.* 15:6810–6821.

Labeit, S., and B. Kolmerer. 1995. Titins—giant proteins in charge of muscle ultrastructure and elasticity. *Science.* 270:293–296.

Li, H., and J. M. Fernandez. 2003. Mechanical design of the first proximal Ig domain of human cardiac titin revealed by single molecule force spectroscopy. *J. Mol. Biol.* 334:75–86.

Li, H., W. A. Linke, A. F. Oberhauser, M. Carrion-Vazquez, J. G. Kerkviliet, H. Lu, P. E. Marszalek, and J. M. Fernandez. 2002. Reverse engineering of the giant muscle protein titin. *Nature.* 418:998–1002.

Lindahl, E., B. Hess, and D. van der Spoel. 2001. GROMACS 3.0: a package for molecular simulation and trajectory analysis. *J. Mol. Model.* 7:306–317.

Linke, W. A., and J. M. Fernandez. 2002. Cardiac titin: molecular basis of elasticity and cellular contribution to elastic and viscous stiffness components in myocardium. *J. Muscle Res. Cell Motil.* 23:483–497.

Lu, H., B. Isralewitz, A. Krammer, V. Vogel, and K. Schulten. 1998. Unfolding of titin immunoglobulin domains by steered molecular dynamics simulation. *Biophys. J.* 75:662–671.

Lu, H., and K. Schulten. 2000. The key event in force-induced unfolding of titin's immunoglobulin domains. *Biophys. J.* 79:51–65.

Marszalek, P. E., H. Lu, H. B. Li, M. Carrion-Vazquez, A. F. Oberhauser, K. Schulten, and J. M. Fernandez. 1999. Mechanical unfolding intermediates in titin modules. *Nature.* 402:100–103.

Mayans, O., P. F. M. van der Ven, M. Wilm, A. Mues, P. Young, D. O. Fürst, M. Wilmanns, and M. Gautel. 1998. Structural basis for activation of the titin kinase domain during myofibrillogenesis. *Nature.* 395:863–869.

McElhinny, A. S., K. Kakinuma, H. Sorimachi, S. Labeit, and C. C. Gregorio. 2002. Muscle-specific RING finger-1 interacts with titin to regulate sarcomeric M-line and thick filament structure and may have nuclear functions via its interaction with glucocorticoid modulatory element binding protein-1. *J. Cell Biol.* 157:125–136.

Metropolis, N., A. W. Rosenbluth, M. N. Rosenbluth, A. H. Teller, and E. Teller. 1953. Equation of state calculations by fast computing machines. *J. Chem. Phys.* 21:1087–1092.

Miller, G., H. Musa, M. Gautel, and M. Peckham. 2003. A targeted deletion of the C-terminal end of titin, including the titin kinase domain, impairs myofibrillogenesis. *J. Cell Sci.* 116:4811–4819.

Nicholas, G., M. Thomas, B. Langley, W. Somers, K. Patel, C. F. Kemp, M. Sharma, and R. Kambadur. 2002. Titin-cap associates with, and regulates secretion of, Myostatin. *J. Cell Physiol.* 193:120–131.

Nicholls, A., K. A. Sharp, and B. Honig. 1990. DelPhi V3.0. Columbia University, New York.

Paci, E., and M. Karplus. 1999. Forced unfolding of fibronectin type 3 modules: an analysis by biased molecular dynamics simulations. *J. Mol. Biol.* 288:441–459.

Pizon, V., A. Lakovenko, P. F. M. van der Ven, R. Kelly, C. Fatu, D. O. Fürst, E. Karsenti, and M. Gautel. 2002. Transient association of titin and myosin with microtubules in nascent myofibrils directed by the MURF2 RING-finger protein. *J. Cell Sci.* 115:4469–4482.

Rief, M., M. Gautel, F. Oesterhelt, J. M. Fernandez, and H. E. Gaub. 1997. Reversible unfolding of individual titin immunoglobulin domains by AFM. *Science.* 276:1109–1112.

Rief, M., M. Gautel, A. Schemmel, and H. E. Gaub. 1998. The mechanical stability of immunoglobulin and fibronectin III domains in the muscle protein titin measured by atomic force microscopy. *Biophys. J.* 75:3008–3014.

Rief, M., and H. Grubmüller. 2002. Force spectroscopy of single biomolecules. *Chemphyschem.* 3:255–261.

Rief, M., J. Pascual, M. Saraste, and H. E. Gaub. 1999. Single molecule force spectroscopy of spectrin repeats: Low unfolding forces in helix bundles. *J. Mol. Biol.* 286:553–561.

Rohs, R., C. Etchebest, and R. Lavery. 1999. Unraveling proteins: A molecular mechanics study. *Biophys. J.* 76:2760–2768.

Trinick, J., and L. Tskhovrebova. 1999. Titin: A molecular control freak. *Trends Cell Biol.* 9:377–380.

Tskhovrebova, L., and J. Trinick. 2003. Titin: Properties and family relationships. *Nat. Rev. Mol. Cell Biol.* 4:679–689.

Tskhovrebova, L., J. Trinick, J. Sleep, and R. M. Simmons. 1997. Elasticity and unfolding of single molecules of the giant muscle protein titin. *Nature.* 387:308–312.

van Gunsteren, W. F., S. R. Billeter, A. A. Eising, P. H. Hünenberger, P. Krüger, A. E. Mark, W. R. P. Scott, and I. G. Tironi. 1996. Biomolecular Simulation: The GROMOS96 Manual and User Guide. Vdf Hochschulverlag AG an der ETH Zürich, Zürich, Switzerland.

Vriend, G. 1990. WHAT IF—a molecular modeling and drug design program. *J. Mol. Graph.* 8:52–56.

Williams, P. M., S. B. Fowler, R. B. Best, J. L. Toca-Herrera, K. A. Scott, A. Steward, and J. Clarke. 2003. Hidden complexity in the mechanical properties of titin. *Nature.* 422:446–449.

Zhang, F. M., A. Strand, D. Robbins, M. H. Cobb, and E. J. Goldsmith. 1994. Atomic structure of the MAP Kinase ERK2 at 2.3 Å resolution. *Nature.* 367:704–711.